

Robust surface superconductivity and vortex lattice in the Weyl semimetal γ -PtBi₂

Jose Antonio Moreno,¹ Pablo García Talavera,¹ Edwin Herrera,¹ Sara López Valle,¹ Zhuoqi Li,^{2,3} Lin-Lin Wang,^{2,3} Sergey Bud'ko,^{2,3} Alexander I. Buzdin,⁴ Isabel Guillamón,¹ Paul C. Canfield,^{2,3} and Hermann Suderow¹

¹*Laboratorio de Bajas Temperaturas y Altos Campos Magnéticos,*

Departamento de Física de la Materia Condensada,

Instituto Nicolás Cabrera and Condensed Matter Physics Center (IFIMAC),

Unidad Asociada UAM-CSIC, Universidad Autónoma de Madrid, E-28049 Madrid, Spain

²*Department of Physics and Astronomy, Iowa State University, Ames, Iowa 50011, USA*

³*Ames National Laboratory, Iowa State University, Ames, Iowa 50011, USA*

⁴*University Bordeaux, LOMA UMR-CNRS 5798, F-33405 Talence Cedex, France*

The layered compound γ -PtBi₂ is a topological semimetal with Fermi arcs at the surface joining bulk Weyl points. Recent work has found a peculiar surface superconducting state with a critical temperature two orders of magnitude larger than the bulk value. However, no superconducting vortices have been identified, raising questions about the robustness of the phase coherence in this new surface superconducting state. Here we measure the superconducting gap and visualize the vortex lattice through very low temperature Scanning Tunneling Microscopy (STM). We find vortices that are anomalously mobile and show that the extremely weak electrostatic interaction between the vortex charge and the STM tip is sufficient to drag the vortices of the surface superconductor. Our results show that surface superconductivity with $T_c = 2.9$ K and $H_{c2} \approx 1.8$ T is extraordinarily robust in γ -PtBi₂. Furthermore, quasiparticle scattering is enhanced at the position in the reciprocal space of the Fermi arcs, suggesting a connection between Weyl points and surface superconductivity.

Many semimetals present Weyl or Dirac nodes in their electronic band structures [1, 2]. The bulk-boundary correspondence often dictates the presence of topologically protected bound states at the surface. This is particularly interesting when it occurs with electron-hole symmetric quasiparticles in a superconductor, because it allows to engineer systems providing Majorana modes [3]. However, few of these semimetals are superconductors in the bulk. This has lead to proposals to study heterostructures consisting of a thin layer of a topological semimetal on top of a bulk superconductor [2, 4–8]. Superconductivity is then induced in the surface state of the semimetal by proximity. Contrasting these proposals, it could also happen that superconductivity is intrinsically realized on the very same topologically protected surface state of a bulk material with Dirac or Weyl nodes [9–11]. Recent experiments and calculations suggest that this situation could be realized in the layered Weyl semimetal γ -PtBi₂ [12–17].

γ -PtBi₂ crystallizes in a layered trigonal structure without inversion symmetry [18]. The band structure contains wide bands crossing the Fermi level at the upper and lower borders of the Brillouin zone. However, the center of the Brillouin zone is gapped. This provides a semimetallic character showing peculiar transport properties as a huge and non-saturating magnetoresistance [19]. The electronic band structure contains Weyl points at approximately 50 meV above the Fermi level [1, 2, 19]. The calculated electronic band structure agrees well with the angle resolved photoemission (ARPES), quasiparticle scattering (QPI) and quantum oscillations experiments [12, 17, 20, 21]. Furthermore, ARPES finds Fermi arcs in surface bands located close to the projection of the Weyl points to the surface plane [12, 20]. At the same time, indications for surface superconductivity with critical temperatures T_c well above 10 K, strongly enhanced

with respect to the bulk ($T_c \sim 0.4$ K) [18, 22, 23] and presenting superconducting gap values of several tens of meV have been proposed based on ARPES and Scanning Tunneling Microscopy (STM) [12–17]. However, the features in the density of states observed with STM provide widely different values of the superconducting gap and recent ARPES measurements do not show any signature of superconducting gap opening on the Fermi arcs within an energy range down to below 1 meV [15, 20]. What is more, the observed gaps close to the Fermi level persist up to very strong magnetic fields (up to 12 T) and there are no reported observations of a vortex lattice nor of the Josephson effect [15, 24]. To better understand the eventual connection of superconductivity and Fermi arcs, it is important to establish the basic properties of surface superconductivity in γ -PtBi₂.

We use here dilution refrigerator STM under magnetic fields to study γ -PtBi₂. We find homogeneous superconductivity down to atomic scale with a critical temperature of $T_c = 2.9$ K and the gap size and temperature dependence following BCS theory. We observe superconducting vortices and study the behavior of the vortex lattice as a function of magnetic field and temperature, finding an anomalously high vortex mobility which is due to the exotic two-dimensional character of superconductivity. QPI shows features of the Fermi arcs at the superconducting quasiparticle peaks.

High-quality single crystals of γ -PtBi₂ were grown using a Bi-rich flux [20], as described in the Supplementary Material [25]. When probed macroscopically either by resistivity or by magnetization, there are no hints of bulk superconductivity down to 1.8 K. The residual resistance ratio is of $RRR \sim 245$, showing that the crystals have minimal disorder scattering. We used a dilution-refrigerator STM with an energy resolution below 8 μ eV described in

Refs. [26, 27], and the data treatment software described in Refs. [28–30]. Further details on the STM data acquisition are described in the Supplementary Material [25]. The cleaving plane is located in between two Bi layers, as shown in Fig. 1 (a). The two possible cleaving surfaces present a trigonal arrangement of Bi atoms, one in which Bi atoms located at two nonequivalent sites (Bi_1 and Bi_2 , termination A) form intertwined corrugated hexagons, and another where the Bi are located on a single plane (Bi_3 , termination B). The resulting STM topographic images show hexagonal patterns (Fig. 1(b,c)), characteristic of each termination. Both terminations provide the same superconducting and vortex lattice properties, described below.

In Fig. 1(e) we show a typical current vs voltage curve for $\gamma\text{-PtBi}_2$ at 0.1 K obtained on atomically flat areas. We note that the current is linear as a function of the voltage, suggesting excellent metallic behavior. We also note the clear and small superconducting gap that opens and a zero current inside the gap. To visualize this better, we show the tunneling conductance vs bias voltage in Fig. 1(f). We find large quasiparticle peaks and zero density of states inside the gap. We can fit the tunneling conductance using a modified BCS density of states, with $\text{DOS}(E) \propto \sum_i \gamma_i(\Delta_i) \text{Re}\left(E/\sqrt{E^2 - \Delta_i^2}\right)$, convoluted with the derivative of the Fermi function at 0.1 K. For a perfectly isotropic s-wave BCS superconductor with gap Δ_{BCS} , $\gamma_i(\Delta_i) = 1$ when $\Delta_i = \Delta_{\text{BCS}}$ and zero elsewhere. Quite often, however, the superconducting gap is not perfectly homogeneous and there is a certain distribution of gap values over the Fermi surface [31–36]. We find here a Gaussian distribution centered around $\Delta_0 = 0.48$ meV with a width of 0.07 meV.

The spatial dependence of the superconducting tunneling conductance at atomic scale is shown in Fig. 2(a-c). The topography shown in Fig. 2(a) provides a typical atomically resolved STM image, containing a few defects, which appear as atomic size adatoms or interstitials (white spots) and as atomic vacancies (black spots). In Fig. 2(b) we represent a line scan of the height measured by STM. We see that the atomic corrugation is small, of a few pm. At the atomic size defects, there are peaks or troughs in the surface of a few tens of pm. Along the whole path, the superconducting gap remains of the same size (Fig. 2(c)). The defects do not produce visible states at low energies well inside the superconducting gap.

The temperature dependence of the superconducting tunneling conductance is shown in Fig. 2(d,e). We can fit the whole temperature dependence using the $\text{DOS}(E)$ discussed previously, convoluted by the derivative of the Fermi function at the temperature of the measurement, without any adjustment parameters up to about 1 K. Above that temperature, the value of the peak is reduced in $\gamma_i(\Delta_i)$, which gives the $\text{DOS}(E)$ provided in the right panel of Fig. 2(d). We plot the peak position in $\gamma_i(\Delta_i)$ as a function of temperature in Fig. 2(e) and find an excellent agreement with BCS theory (red line) up to the critical temperature of $T_c = 2.9$ K. With this value of T_c we can

estimate the zero temperature superconducting gap using BCS theory, and we find $\Delta_{\text{BCS}} = 1.76 k_B T_c = 0.44$ meV, which coincides with Δ_0 better than within 10%.

We present the behavior of superconducting vortices, obtained by mapping the zero bias conductance as a function of the position, for different values of the magnetic field and at 0.1 K in Fig. 3. In Fig. 3(a) we show an isolated vortex. The tunneling conductance outside the vortex is close to its zero field value, and at the core of the vortex we observe a flat tunneling conductance (Fig. 3(b)).

In Fig. 3(c) we show a zero bias tunneling conductance map obtained at 0.4 T which is representative for the typical vortex lattice behavior we observe. In Fig. 3(d) we show the corresponding topography, we can identify atomically flat terraces on the upper part of the topography and nanometer-sized flakes which surge on top of the atomically flat terraces on the lower part. Concurrently, on the upper part of the zero bias tunneling conductance map (Fig. 3(c)) we find a homogeneous superconducting tunneling conductance, with curves similar to those found at zero field. On the lower part of Fig. 3(c) we observe, by contrast, the vortex lattice. The tunneling conductance curves in and outside vortices are similar to those shown in Fig. 3(a,b). We note that we cannot distinguish between the tunneling conductance outside vortex cores on nanometer-sized flakes and on the atomically flat areas. This behavior is found all over the surface of $\gamma\text{-PtBi}_2$ in hundreds of fields of view, in different samples, and for different surface terminations on the atomically flat terraces—atomically flat terraces present no trace of vortices, whereas nanometer-sized flakes provide a neat vortex lattice.

We show in Fig. 3(e,f) a zero bias tunneling conductance map on a different field of view and for two values of the magnetic field. We see that the vortex density increases with the magnetic field. The intervortex distance as a function of the magnetic field (Fig. 3(g)) follows Abrikosov behavior for a hexagonal vortex lattice [37, 38]. Indeed, although the vortex lattice shows some degree of disorder, the Fourier transform mostly presents a hexagonal pattern (insets of Fig. 3(e,f)). By extrapolating the zero bias tunneling conductance outside vortices to high fields, we estimate an upper critical field $H_{c2} = 1.8$ T, applied perpendicular to the surface, which provides an in-plane coherence length of about $\xi_{a,b} = 13$ nm.

From our result, we see that vortices must be found all over the sample surface, including atomically flat terraces, because the very large magnetic fields we apply here inherently create vortices in a superconductor. The apparent absence of vortices in STM on flat terraces should be due to peculiar vortex pinning properties.

To better understand this point, let us consider the electrostatic interaction of vortices with a non-magnetic tip. As shown in Ref. [39], there is a redistribution of charge due to the differences in the chemical potential between superconducting and normal quasiparticles. Metallic screening does not fully eliminate the charge. This

results in an electric dipole p oriented perpendicular to the surface whose strength is of the order of $p \sim ed$ where e is the elementary charge and $d \sim 1 \text{ \AA}$ (which gives $p \sim 1 \text{ D}$, one Debye, see Fig. 11 in the Supplementary Material). Such a minute electric dipole has been often considered previously and has an influence in several properties of superconductors, such as the Hall effect in the mixed state [40–44]. To estimate the force generated by the electric field of the tip E on the vortex, we first consider the corresponding interaction energy, $U \sim Ep$. The dipole sits on the vortex core, but its field extends over a distance of order of the superconducting coherence length $\sim \xi_{a,b}$. We now consider a tip which is at a distance smaller than $\xi_{a,b}$ and is blunt and large in size (see for a schematic picture Fig. 11 in the Supplementary Material). The effective electric field is then $E \sim V/\xi_{a,b}$, where V is the voltage applied to the tip. We can then estimate the force acting on the vortex as $F_E \sim U/\xi_{a,b} \sim Vp/\xi_{a,b}^2$. For $V \sim 0.1 \text{ V}$, $\xi_{a,b} \sim 10 \text{ nm}$ we obtain $F_E \sim 10 \text{ fN}$.

The pinning force F_p can be roughly estimated by considering the free energy per unit volume from the thermodynamic critical field and the vortex volume [45]. Estimates are often of order of 10^{-6} N/m [45, 46]. In $\gamma\text{-PtBi}_2$, the bulk is normal, which implies that superconductivity is restricted to a small layer close to the surface. Taking a thickness for the superconducting layer of 1 nm , we estimate $F_{p1} \sim 1 \text{ fN}$ (see Fig. 11 in the Supplementary Material), which is one order of magnitude below our estimate of F_E . If superconductivity is restricted to a thin layer occupied by a surface band, the thickness should be similar or smaller than a unit cell size, which is of 0.617 nm along the c -axis.

On the other hand, on nanometer-sized flakes, the vortex length increases, which also increases the pinning force, up to $F_{p2} > F_E$.

Thus, we conclude that on atomically flat surfaces, $F_{p1} < F_E$ and vortices move together with the tip and remain undetected (further details provided in the Supplementary Material). However, when $F_{p2} > F_E$, the vortex lattice remains pinned and does not move during scanning. Then, STM reveals the presence of vortices.

Such a highly mobile vortex lattice should be very sensitive to temperature. Indeed, increasing temperature to about 2 K , well below T_c , leads to a completely blurred vortex configuration (see Supplementary Material), similar to the features observed with STM in vortex liquid phases [47–51].

It is interesting to remark that the anisotropy of the upper critical field measured in thin flakes of $\gamma\text{-PtBi}_2$ suggests that the superconducting coherence length is twenty times smaller along the c -axis than in plane, $\xi_{a,b} \sim 20 \xi_c$ [22]. Superconductivity is thus indeed restricted to a surface layer and F_{p1} is possibly even smaller than estimates given above. Furthermore, the coherence length perpendicular to the surface ξ_c is so small, that the in-gap density of states induced by proximity from the normal bulk is practically absent in the superconducting density of states at the surface.

Thus, we have established that robust superconductivity with $T_c = 2.9 \text{ K}$ exists on the surface of $\gamma\text{-PtBi}_2$. STM provides a spatially continuous superconducting gap with a temperature dependence following BCS theory. In addition, we show that the Cooper pair wave function is uniquely valued, through the observation of flux quantization on the vortex lattice. Finally, as shown in the Supplementary Material, we observe the Josephson effect when using a superconducting tip.

To investigate the relationship between superconductivity and the Fermi arcs found in ARPES [12, 20], we have performed QPI maps of the tunneling conductance on an atomically flat terrace with sufficient atomic size defects to obtain scattering (on the area shown in Fig. 2(a)). As shown previously, the tunneling conductance vanishes within the gap, so that the tunneling conductance maps inside the gap are essentially zero. However, exactly at the quasiparticle peaks position, we find clear signatures of QPI. This suggests that the superconducting density of states varies spatially through quasiparticle scattering. This variation shows changes in the reciprocal space gap structure induced by impurity scattering. We show the Fourier transform of the tunneling conductance map at $V = -\Delta_0/e$ in Fig. 4(a). A similar result is found for $V = +\Delta_0/e$. We find several scattering wave vectors agreeing with previous QPI and ARPES experiments at energies above the superconducting gap edge [17, 20]. By comparing with DFT (Fig. 4(b,c)) we find, at the superconducting gap edge, scattering wave vectors (q_1 , q_2 , q'_2 and q_3) which coincide with wave vectors joining Fermi arcs that connect the projections of Weyl points to the surface.

Whereas we observe superconductivity for temperatures below 3 K , compatible with the recent ARPES experiments of Ref. [20], the temperature range for earlier claims of superconductivity in $\gamma\text{-PtBi}_2$ is reported to be even far above the T_c we observe here [12–16]. The repeated observation of atomically flat areas in our experiment, always presenting the same gap values, shows that the superconducting properties observed here must be due to intrinsic two-dimensional superconductivity at the surface. It remains unclear what is causing the surface superconductivity. It could be small shifts in the band structure leading to enhanced density of states and/or changes in the phonon structure close to the surface [9, 10]. Interestingly, monolayer $\gamma\text{-PtBi}_2$ has been proposed to be a ferroelectric metal due to phonon softening [52]. Furthermore, it has been recently proposed that normal metals with Weyl points can show phonon mediated surface superconductivity [11]. As we have now shown that such two-dimensional superconducting state exists and is robust, it is also interesting to ask about the relationship with the topological properties of the electronic band structure.

Our QPI measurements show that the superconducting gap opens at the Fermi arcs. For superconducting Fermi arcs that are projections of bulk Weyl points, Majorana modes are expected inside vortices. These should

be visible by a peak in the tunneling conductance inside the vortex core [2–8]. But even in absence of Majorana modes, superconductors in the clean limit present pronounced peaks in the tunneling conductance inside vortex cores [34, 50, 53–57]. Their absence in Fig. 3(b) suggests that the electronic mean free path on the nanometer-sized flakes is of the order or slightly smaller than the superconducting coherence length, $\xi_{a,b} = 13$ nm. This is considerably smaller than the bulk mean free path, which is of 200 nm or larger, as estimated from the residual resistance ratio of our samples. Thus, the two-dimensional electronic band structure at the surface of the nanometer-sized flakes is sufficiently well developed locally to carry surface superconductivity, but the mean free path is not sufficiently large to provide vortex cores with localized states inside.

Vortices on atomically flat terraces, where we also took the QPI data showing the connection between superconductivity and Fermi arcs (Fig. 4(a)), are probably in the clean limit and carry bound states, which could realize Majorana modes [11]. The charge of vortices carrying Majorana modes has been investigated theoretically. It is found that, depending on the different possible chiral p-wave superconducting states, vortices carrying Majorana fermions might be uncharged or charged [58, 59]. The latter are expected to present a considerably enhanced charge with respect to conventional s-wave superconductors [58, 59]. Our data suggest that the vortices on atomically flat terraces carry a substantial charge and have therefore a strong interaction with the tip.

In summary, we have found robust surface superconductivity in γ -PtBi₂ with a T_c much larger than the bulk and which is connected to the Fermi arcs joining the projection of bulk Weyl points. The two-dimensional superconductivity confers exceptional vortex mobility, an aspect which should be taken into account to address unconventional superconductivity in topological edge states and will be of help to design experiments on interaction among unconventional bound states in superconductors.

ACKNOWLEDGMENTS

We acknowledge support by the Spanish Research State Agency (PID2023-150148OB-I00, TED2021-130546BI00, PDC2021-121086-I00 and CEX2023-001316-M), the European Research Council PNICTEYES through grant agreement 679080 and VectorFieldImaging Grant Agreement 101069239, the EU through grant agreement No. 871106 and by the Comunidad de Madrid through projects TEC-2024/TEC-380 “Mag4TIC”. We acknowledge the “QUASURF” project [SI4/PJI/2024-00199] funded by the Comunidad de Madrid through the direct grant agreement for the promotion and development of research and technology transfer at the Universidad Autónoma de Madrid. We have benefited from collaborations through EU program Cost CA21144 (superqumap), and from SEGAINVEX at UAM in the design and con-

struction of STM and cryogenic equipment. Work done at Ames National Laboratory (PCC, SLB, LLW, ZL) was supported by the U.S. Department of Energy, Office of Basic Energy Science, Division of Materials Sciences and Engineering. Ames National Laboratory is operated for the U.S. Department of Energy by Iowa State University under Contract No. DE-AC02-07CH11358.

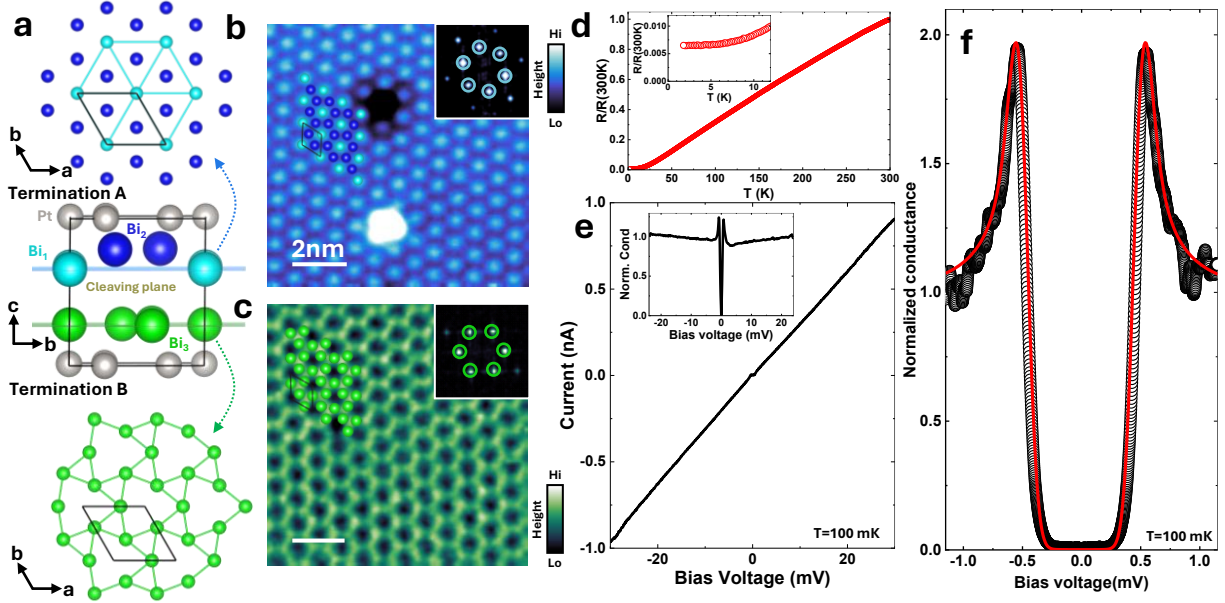


Figure 1. (a) Unit cell of γ -PtBi₂ (space group No. 157), with Bi atoms in blue and green and Pt atoms in grey. The system is composed of layers where Pt is surrounded by Bi, so that the surface after cleaving is always composed of Bi. The Bi can however hold two different terminations, one where inequivalent Bi atoms form a buckled hexagonal surface (Bi₁ and Bi₂, termination A) and another one in which the Bi forms a single plane (Bi₃, termination B). (b,c) Atomically-resolved STM topography taken on the two possible terminations of γ -PtBi₂. White scale bar corresponds to 2 nm. Colormap is shown to the right. Inset shows the FFT with the Bragg peaks marked with circles. The atomic arrangement of Bi atoms is schematically shown by colored circles in the main panels. (d) Resistivity measurement as a function of temperature on γ -PtBi₂ showing no traces of superconductivity down to 1.8 K and a residual resistance ratio exceeding 200. (e) Typical current vs voltage curve obtained with a normal tip. Inset shows conductance vs voltage curve in the same voltage range. We remark that the behavior is completely metallic. A superconducting gap opens below $\Delta_0 = 0.48$ mV. The temperature is of $T = 0.1$ K, bias voltage $V = 30$ mV, and setpoint current $I = 1$ nA. (f) Tunneling conductance vs bias voltage obtained with the same parameters as in (e) and $V = 1.2$ mV. Red line is a fit to a BCS density of states with a small distribution of gap values described in the text and in Fig. 2.

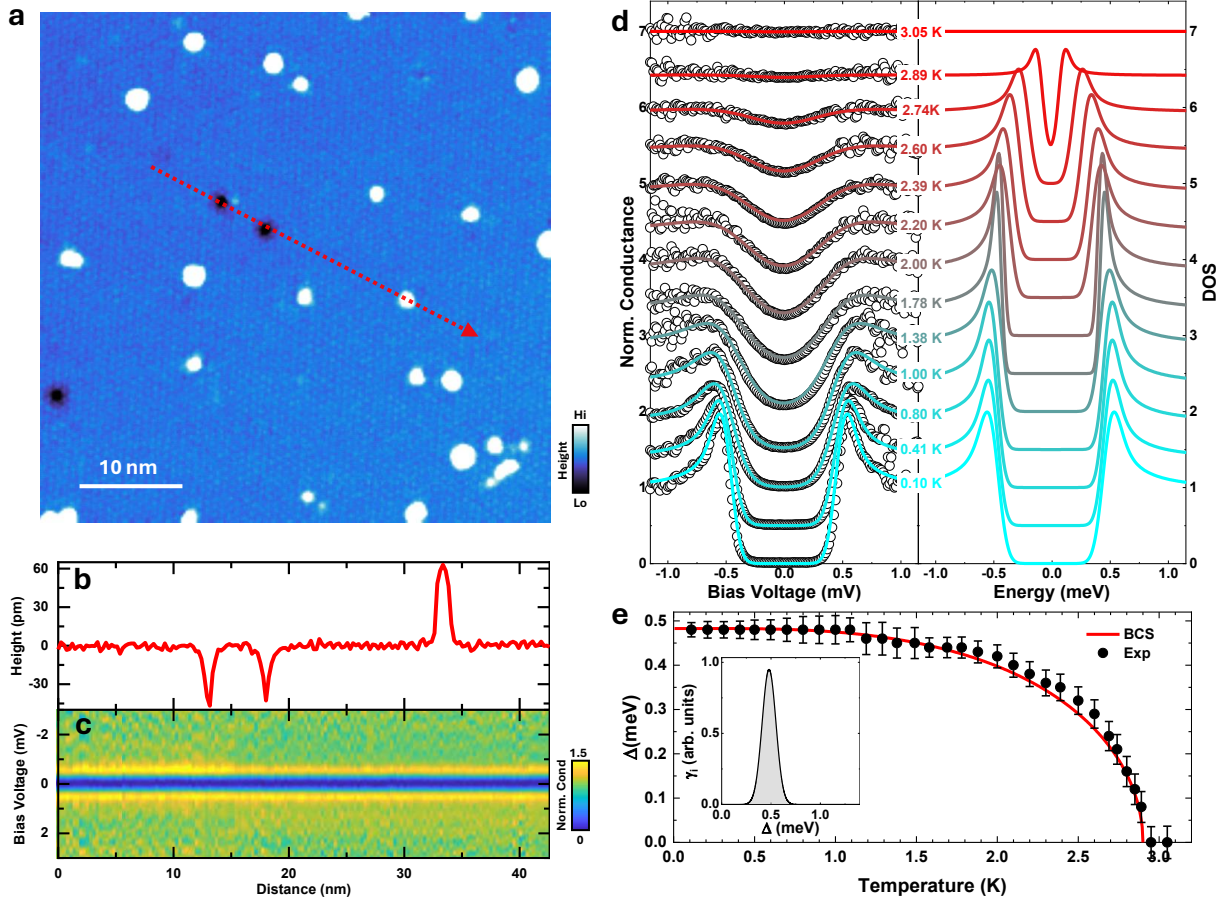


Figure 2. (a) Atomically-resolved STM topography presenting a few defects on termination A. White scale bar corresponds to 10 nm. Colormap is shown to the right. (b) Profile along the red arrow on the topography shown in (a). (c) Conductance as a function of bias voltage taken simultaneously as the topography, following the same profile as (b). Colormap is shown to the right. We see that the superconducting gap is homogeneous over the whole surface and over defects. (d) On left panel we show the tunneling conductance vs bias voltage as a function of temperature (dots) and calculated conductance curves obtained after convoluting the BCS DOS (shown on the right panel) with the derivative of the Fermi function at each temperature, as described in the text. Curves are shifted vertically for clarity. (e) Temperature dependence of the superconducting gap, obtained as described in the text. The solid line is the BCS temperature dependence. Inset shows the Gaussian distribution $\gamma_i(\Delta_i)$ centered around $\Delta_0 = 0.48$ meV with a width of 0.07 meV used for the T=100 mK fit.

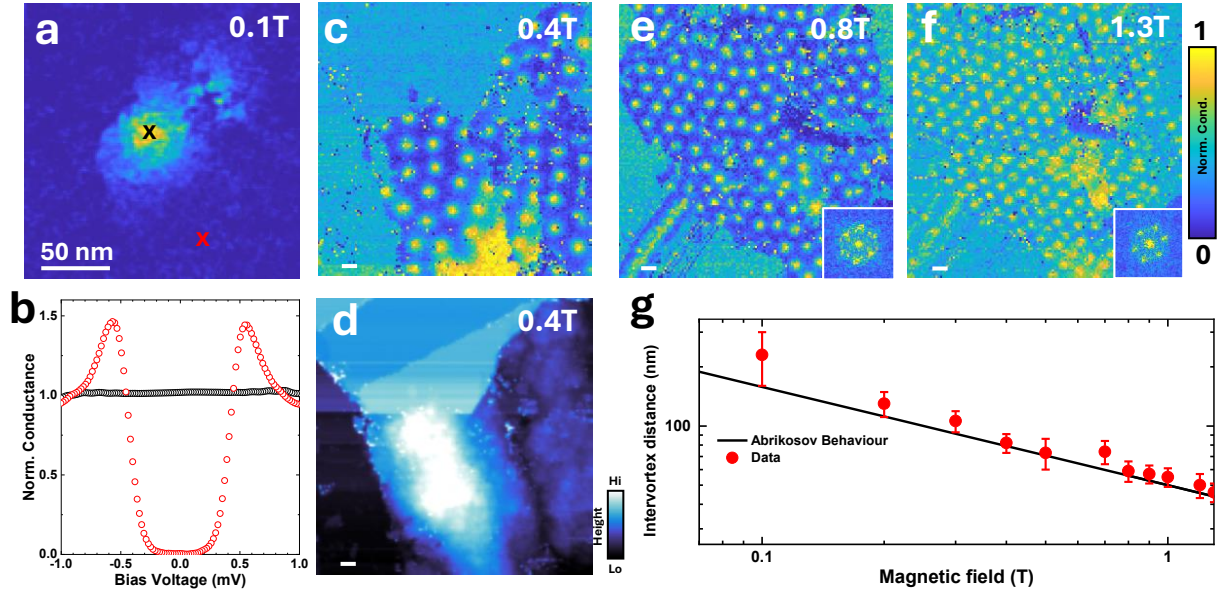


Figure 3. (a) Zero-bias tunneling conductance map of a single vortex at 0.1 T. (b) Normalized tunneling conductance curves obtained at the core of the vortex (black dots, black cross in (a)) and away from the vortex (red dots, red cross in (a)). (c,e,f) Tunneling conductance maps at zero bias showing the vortex lattice as a function of the magnetic field at 0.4 T (c), 0.8 T (e), and 1.3 T (f). (e,f) maps were taken on the same field of view. White scale bars correspond to 50 nm in main panels. Insets in (e,f) on the bottom right corner show the Fourier transform, giving a hexagonal set of peaks. (d) Topography taken simultaneously to the conductance map shown in (c). Notice that vortices are not observed on atomically flat surfaces. (g) Intervortex distance as a function of the magnetic field is shown as red disks. The error bars are obtained by Delaunay triangulating vortex positions and measuring the width of the distribution of distances. Solid line corresponds to the Abrikosov prediction for an hexagonal vortex lattice $d_{vortex} \sim 1.075 \left(\frac{\Phi_0}{B} \right)^{1/2}$.

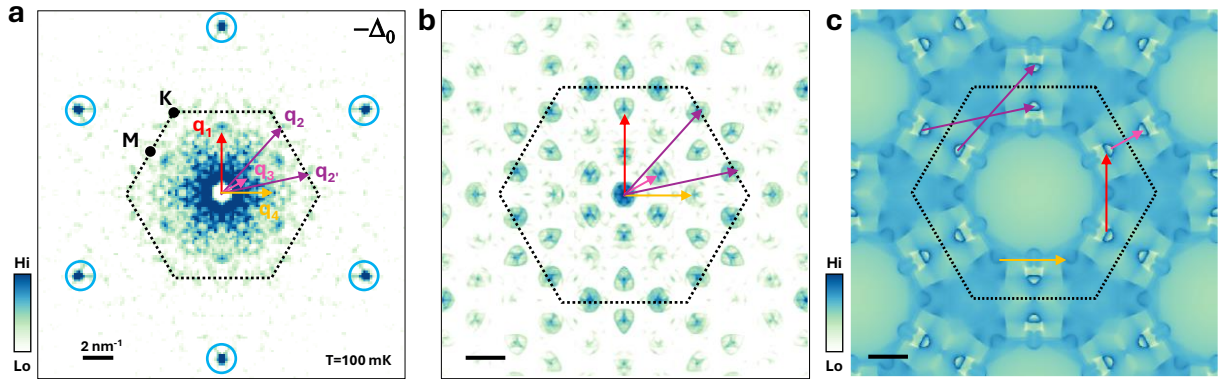


Figure 4. (a) Quasiparticle interference pattern in γ -PtBi₂ measured on the region shown in Fig. 2 (a). The scattering intensity is shown on a color scale, following the bar on the left. The dashed contour is the first Brillouin zone and K and M denote high symmetry points. We mark the position of Bragg peaks with blue circles. We mark relevant scattering wavevectors q_1 , q_2 , q_2' , q_3 and q_4 by colored arrows. The pattern is obtained from a tunneling conductance map at the bias voltage of the BCS quasiparticle peak, $V = -\Delta_0/e = -0.48$ mV. (b) Joint density of states obtained from density functional theory (DFT) calculations of the band structure at the Fermi surface (shown in (c)). The colored arrows are the scattering wave vectors found in (a). (c) Fermi surface of γ -PtBi₂. Arrows show the scattering wave vectors found in (a). The Brillouin zone is shown by a dashed black line in (b,c).

SUPPLEMENTARY MATERIAL OF: ROBUST SURFACE SUPERCONDUCTIVITY AND VORTEX LATTICE IN THE WEYL SEMIMETAL γ -PTBI₂

I. SINGLE CRYSTAL GROWTH OF γ -PTBI₂

Elemental Bi and Pt were combined in a Bi80-Pt20 ratio and placed in a fritted, alumina crucible set (available as Canfield Crucible Set or CCS) [60, 61]. The CCS was sealed into an amorphous silica tube and placed into a box furnace [62]. The ampoule was then heated to 1000 °C over 5 hours, held at 1000 °C for 5 hours, cooled to 700 °C over 4 hours and then slowly cooled to 440 °C over 146 hours. At 440 °C, above the reported 420 °C transformation temperature to the cP12/Pa-3 phase of PtBi₂ [ASM phase diagram entry 979935 for Bi-Pt binary phase diagram] [63], the ampoule was removed from the furnace and the excess, Bi-rich solution was decanted [62]. Once the ampoule cooled to room temperature it was opened and large, cleanly faceted plates of hP9/P-3 (space group no. 157) PtBi₂ were revealed. X-ray diffraction measurements taken ground single crystals confirmed the correct, high temperature phase and further illustrated the stability of the phase at room temperature [20].

II. COMPARISON WITH THE SUPERCONDUCTING PROPERTIES FOUND IN LITERATURE

Bulk resistivity measurements have found a transition to the superconducting state at ~ 0.6 K-1.1 K [13, 18] that can be enhanced up to ~ 2.5 K by doping with Rh [18] or by hydrostatic pressure [23]. Thin flakes with a thickness of the order of tens of nanometers have shown a Berezinskii-Kosterlitz-Thouless transition at ~ 300 mK [22]. Techniques probing the surface have found a plethora of different critical temperatures ranging from ~ 3 K (point-contact) [14], to ~ 6 K (SQUID on tip) [15] and to ~ 8 -14 K [12] (ARPES). Most remarkably, STM measurements found superconducting gaps compatible with a T_c of the order of ~ 80 K [15] and a $H_{c2} > 15$ T. However, superconducting properties probed in Ref. [15] were extremely inhomogeneous and even contained non-superconducting regions [17]. Furthermore, the vortex lattice could not be observed in Ref. [15] despite having performed measurements under high magnetic fields. Other work in γ -PtBi₂ did not find evidence for superconductivity in STM [16] and ARPES (down to 3 K) [20].

III. FURTHER ASPECTS OF THE STM EXPERIMENT

We cleaved samples in-situ at 4.2 K or below. Samples were cleaved by gluing a post of alumina on top of the samples and hitting the alumina by moving the sample holder below a beam. We measured hundreds of fields of

view in three different samples, obtaining the behavior discussed in the main text in each of them.

We used tips of Pt-Ir, unless in the experiment with superconducting tip, where we used Pb tips. To prepare and clean the tips we used the tip preparation methods described in Ref. [64, 65], which essentially consists of moving the tip towards a sample of the same material as the tip and making controlled repeated indentations.

We would like to remark that we usually find a single surface termination when measuring a certain sample of γ -PtBi₂. To obtain data from the two surface terminations, we first cleaved one sample and measured it, finding atomically flat terraces with termination A (Fig. 1 of the main text). The cleaved piece was attached to a rope and was let to fall down to the bottom of the inner vacuum chamber of the dilution refrigerator. We then took this part and mounted it in such a way as to make sure that the upper surface was at the other side as compared with previous experiment. We then cooled again and cleaved the sample again. We found, in that new cleave, always atomically flat terraces with the same B-surface termination, opposite to the previous one (termination B in Fig. 1 of the main text). The shape and superconducting behavior on nanometer-sized flakes was the same for both surface terminations in atomically flat areas.

It is not fully clear why we do not observe atomic resolution on flakes, but instead a surface with a certain corrugation larger than atomic sizes. We speculate that the surface of the flakes is not completely flat. Interestingly, the flat areas on the flakes are sufficiently large so that surface states and superconducting vortices form.

During scanning, the current was most often around 1 nA and the bias voltage of a few mV. We usually present the tunneling conductance normalized to its value well above the superconducting gap edge. Tunneling conductance maps were obtained by cutting the feedback loop at each pixel on the scan area and making a full tunneling conductance vs bias voltage measurement. We also provide DFT calculations, performed as described with detail in the in the next section.

IV. DFT CALCULATIONS

Band structure of γ -PtBi₂ in space group 157 with spin-orbit coupling (SOC) in DFT [66, 67] have been calculated with PBE3 [68] exchange-correlation functional, a plane-wave basis set and projected augmented wave method [69] as implemented in VASP [70, 71]. A Monkhorst-Pack [72] ($8 \times 8 \times 8$) k-point mesh with a Gaussian smearing of 0.05 eV including the Γ point and a kinetic energy cut-off of 230.3 eV have been used. A tight-binding model based on maximally localized Wannier functions [73–75] is constructed to reproduce closely the bulk band structure including SOC in the range of $E_F \pm 2$ eV with Pt *sd* and

Bi p orbitals. The surface spectral function and the QPI pattern are shown as the joint density of states [76] of the semi-infinite surface. These have been calculated with the surface Green's function methods [77, 78] as implemented in WannierTools [79].

V. NANOMETER-SIZED FLAKES

We have imaged the surface of our cleaved samples after STM measurements using high-resolution Scanning Electron Microscopy (SEM) to characterize the origin and composition of the nanometer-sized flakes. In Fig. 5 (a) we show a typical image of several microns showing several step edges and 120° corners, reflecting the trigonal symmetry of the crystal lattice. In Fig. 5 (b) we show a zoom on a flat terrace showing flakes of the length scale we have observed in our STM measurements. We have performed Energy Dispersive electron Spectroscopy (EDS) measurements on some of these objects and on top of the flat defect-free surface to analyze the elemental composition. EDS essentially yields the same composition for all measured spots, i.e, Pt:Bi=1.0 : 2.0 which coincides with the stoichiometric ratio within the experimental uncertainty of ± 0.15 . Many of these flakes are found around step edges and some have a rough hexagonal shape. Possibly these are caused by defects during cleavage.

VI. VORTICES IN γ -PTBI₂

A. Magnetic field history

The observed behavior (absence of a clear vortex lattice and instead the presence of a homogeneous tunneling conductance on atomically flat terraces and vortex lattice in nanometer-sized flakes) is independent on the magnetic field history (field cooling, zero field cooling), the reversal of the direction of the magnetic field, the reversal of the setup bias voltage and the size of the tunneling current down to 0.1 nA.

B. Interaction with nanometer-sized flakes

In Figs. 6,7,8 we present three experiments which we consider interesting, because they provide more information about the nature of the vortex lattice in the nanometer-sized flakes.

In Fig. 6(a) we show a zero-bias conductance map of a single vortex together with the simultaneously-acquired topography in Fig. 6(c). We observe that the vortex is confined to the nanometer-sized flake. In Fig. 6(b,d) we plot the tunneling conductance and topography profiles as a function of the position as the tip moves from the nanometer-sized flake (delimited with white dashed lines in Fig. 6(a,c) onto the atomically flat regions). We see in Fig. 6(b) a fully opened superconducting gap on the

atomically flat terrace and a neat vortex on the nanometer-sized flake.

Another example of an atomically flat surface at an applied magnetic field of 0.5 T is shown in Fig. 7(a). This surface presents a hole on the upper left corner. In Fig. 7(b) we see the result of a first scan. Inside the hole we find a nanometer-sized flake. Although the superconducting gap is perfectly homogeneous over the whole surface, we see the vortices on the nanometer-sized flake within the hole Fig. 7(c). After making several scans, we find the topography shown in Fig. 7(e). The surface inside the hole is now perfectly flat, because the tip motion has changed the position of the nanometer-sized flake, possibly removing it altogether from this field of view. We then see no trace of the vortices Fig. 7(f) and instead a spatially homogeneous superconducting tunneling conductance with the properties discussed in the main text.

Finally, in Fig. 8 we elaborate further on vortex dynamics on the field of view shown in Fig. 3 (e,f) of the main text. In Fig. 8 (a) we show the topography acquired simultaneously with the tunneling conductance map shown in Fig. 3(e) of the main text. In the center of the field of view there is a large nanometer-sized flake. On the bottom left corner (orange square) there is a stripe-like flake separating two atomically flat regions. In Fig. 8(b) we show the tunneling conductance map corresponding to this area. We see that vortices appear blurred and confined to a central line. It is important to note that this stripe-like nanometer-sized flake is smaller in height than the one present on the center of Fig. 8(a). The height profile, shown in Fig. 8(c,d) shows a difference in size of more than an order of magnitude. This implies that vortices length is smaller on the stripe-like nanometer-sized flake, which allows for vortex mobility and produces a one-dimensional blurred feature in the tunneling conductance map. This suggests that there is a gradual evolution with increasing flake height from the free-moving vortices on flat surfaces to the completely pinned vortices on big nanometer-sized flakes.

It remains unclear why the effective length of superconducting vortices extends over larger length scales along the c -axis on flakes as compared to atomically flat areas. γ -PtBi₂ consists of weakly coupled layers of PtBi₂ groups, separated by a van der Waals gap [18]. It could be that the areas where we observe vortices are composed of disordered groups of weakly coupled flakes. Each group will contain surface superconductivity and carry vortices, which interact through their magnetic field. This might allow for the establishment of interactions among two-dimensional surface vortices. We remind that, similarly, pancake vortices are observed with STM on Bi₂Sr₂CaCu₂O_x. There are no reports of electrostatic STM tip-vortex interactions with two-dimensional vortices in Bi₂Sr₂CaCu₂O_x. The magnetic interaction among pancakes at different layers allows for vortex stability and their observation with STM [80, 81].

C. Vortex dynamics temperature dependence

We show the effect of increasing temperature on the vortex lattice in Fig. 9(a-d). The scans are made consecutively and in the same field of view. The nanometer-sized flake slightly changes its lateral size with subsequent scans, but the surface remains large enough to identify the vortex lattice at the applied magnetic field (0.7 T). We see a hexagonal vortex lattice at 0.1 K, which remains but is considerably disordered at 1.2 K. At 1.5 K, there are practically no traces of superconducting vortices, although the average tunneling conductance normalized to its value at high voltages is well below one. This shows that vortices are moving below the tip. At 2 K, the tunneling conductance on the nanometer-sized flake is homogeneous, suggesting thermally activated vortex motion.

Remarkably, the tunneling conductance outside the nanometer-sized flake remains below its value inside. This suggests that vortices have a different dynamics on atomically flat surfaces and on the nanometer-sized flake.

D. Vortex core size as a function of the magnetic field

The extension of vortices is related to the order parameter spatial dependence and, through this, to the coherence length $\xi_{a,b}$. A natural model to gauge the vortex core size C is thus to consider the order parameter slope at the vortex core center, such that $d\Delta/dr|_{r \rightarrow 0} \propto 1/\xi_{a,b} \propto 1/C$. This model is described in Ref. [82]: In a STM measurement we can relate the spatial distribution of the order parameter with the normal DOS $N(r)$ and the tunneling conductance σ using deGennes model [83] and considering that the order parameter must evolve smoothly, i.e., $d\Delta/dr = 0|_{r=L/2}$ at half of the intervortex distance L due to the periodicity of the vortex lattice. The resulting expression is:

$$\sigma = 1 - \frac{\rho^2(1 + \eta^2)}{\rho^2 + \eta^2} \exp\left(\frac{\eta^2(1 - \rho^2)}{1 + \eta^2}\right) \quad (1)$$

where $\rho = r/a$, $\eta = C/a$, and a is the radius of the circular cell we use to approximate the hexagonal Wigner-Seitz cell of the vortex lattice ($a/(L/2) \sim 1.05$) [82]. In Fig. 10 we show the vortex core size C , as obtained from fitting the radially-averaged tunneling conductance along vortex cores to equ. 1 following Ref. [82]. We find that the vortex core size C is slightly decreasing with the magnetic field and tends towards the coherence length $\xi_{a,b} = 13$ nm at the critical field $H_{c2} = 1.8$ T. This behavior is expected for a superconductor with an electronic mean free path of order of $\xi_{a,b}$ [82], confirming the strong reduction of the mean free path on nanometer-sized flakes.

VII. ELECTROSTATIC INTERACTIONS BETWEEN TIP AND VORTEX LATTICE

We illustrate the interaction between tip and sample in Fig. 11. As is well known, a STM is most often blunt, but there is always a small atomic size tip which dominates in the tunneling process, because of the exponential dependence of the tunneling current with distance [84]. We represent the tunneling tip by a small triangular-like tip in Fig. 11. The tunneling current from this tip is shown schematically in red. The overall shape of the tip is however blunt and we represent it by a semi-spherical object with a radius of several nm. Indeed, the electrostatic interaction between tip and sample F_E occurs over a much larger scale than tunneling, which depends on the size of the tip but is typically several nm in diameter [85–90]. The electrostatic interaction between tip and dipoles on the sample contains several components, such as image charges and the actual dipolar interaction [85, 89, 90]. The latter can be, in principle, attractive and repulsive, depending for instance on the sign of the bias. Independently on the sign of the interaction, for a certain electrostatic configuration, there is an equilibrium distribution of vortices below the tip, most often consisting of the vortex lattice confined within the geometry of the capacitor built by the spherical tip (with nm or tens of nm radius). This equilibrium distribution of vortices below the tip is carried when moving the tip.

In practice, the interaction can just lead to changes in the position of a few vortices, because the hexagonal vortex lattice is not perfect and the vortex positions are slightly influenced by small defects. With very weak pinning, we obtain the result shown schematically in Fig. 11(b,c). When we move the tip the equilibrium position some vortices move together with the tip in such a way as to maintain the distribution of charges below the tip. The crux is that the point at which we tunnel is rarely, coinciding with a vortex core, as it is not located at the center of the capacitor built by the tip and the sample. Therefore, in most cases, no signature of vortices can be found from tunneling at the tip's apex.

By contrast, adding additional two-dimensional superconducting layers on top of nanometer-sized flakes, as schematically represented in Fig. 11(d), enhances the effective length of the magnetic vortex. This increases the pinning force, eventually leading to $F_{p2} > F_E$. In that case, we have the situation proposed in Fig. 11(e,f). The vortex lattice on the flakes remains fixed (dark blue on Fig. 11(e,f), $F_{p2} > F_E$), but vortices on the flat two-dimensional surface are moved by the interaction with the tip (light blue on Fig. 11(e,f), $F_{p1} < F_E$).

In a few cases, we observe indeed changes in the density of states on the flat regions. Furthermore, at elevated temperatures and under magnetic fields (Fig. 9(d)), the zero bias tunneling conductance on the atomically flat areas at 0.7 T is higher than the one observed at zero magnetic field and at the temperature of the measurement ($\frac{dI}{dV}_{norm}(V=0, B=0T) = 0.26$ and $\frac{dI}{dV}_{norm}(V=0, B=$

0.7T) = 0.36, where $\frac{dI}{dV}_{norm}$ is the tunneling conductance normalized to its value at high bias). This shows that the atomically flat areas are interspersed with fluctuating vortices with increased temperature.

The electrostatic interaction between tip and sample unveiled here complements previous STM work in semi-conducting materials, where such interactions essentially lead to band-bending and changes in the lateral resolution [89, 90]. In all cases, electrostatics leads to an invasive interaction. In superconductors, the electric field is most often perfectly screened and such interactions have been neglected. But at vortex cores we observe here the unexpected consequence of allowing for vortex motion in sufficiently thin superconductors.

Absence of vortices has been reported previously in highly disordered and very thin films particularly close to the superconductor to insulator transition [91–93]. An enhanced vortex mobility and tip-sample interactions could play a certain role in those observations too.

VIII. STM TUNNELING WITH A SUPERCONDUCTING TIP

To obtain further evidence of the robustness of the superconducting properties of γ -PtBi₂ we performed controlled indentations of the tip into the sample, picking up pieces of γ -PtBi₂. We observed the Josephson effect and traced its evolution when changing the tunneling current. We observed similar behavior as found previously in systems as Pb or Al [64]. There are peaks in the tunneling conductance at twice the superconducting gap and at the superconducting gap, due to Andreev reflection. In addition, there is a pronounced peak at zero bias which evidences the passage of a Cooper pair (Josephson) supercurrent (Fig. 12 (a)). When measuring with a tip of Pb, we also observe a Josephson peak (Fig. 12 (b)) and the features in the tunneling conductance characteristic of tunneling between superconductors with different gap sizes [94].

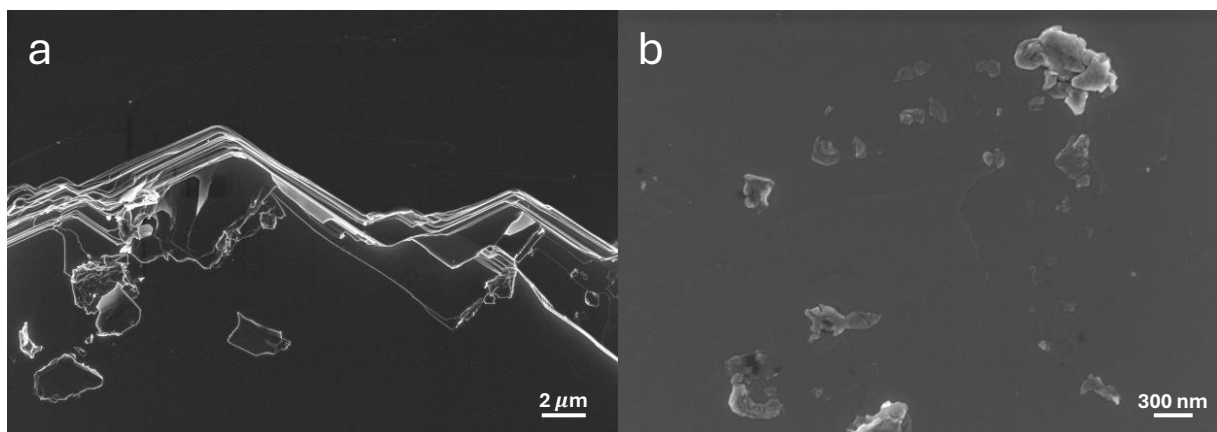


Figure 5. a) Scanning Electron Microscope (SEM) image of the surface of γ -PtBi₂ at an edge of the sample. White scale bar is 2 μ m long. (b) SEM image with higher resolution. White scale bar is 300 nm long. Using Energy Dispersive electron Spectroscopy (EDS), we find a homogeneous composition corresponding to the stoichiometry of γ -PtBi₂ over the whole field of view, including the nanometer-sized flakes shown in (b).

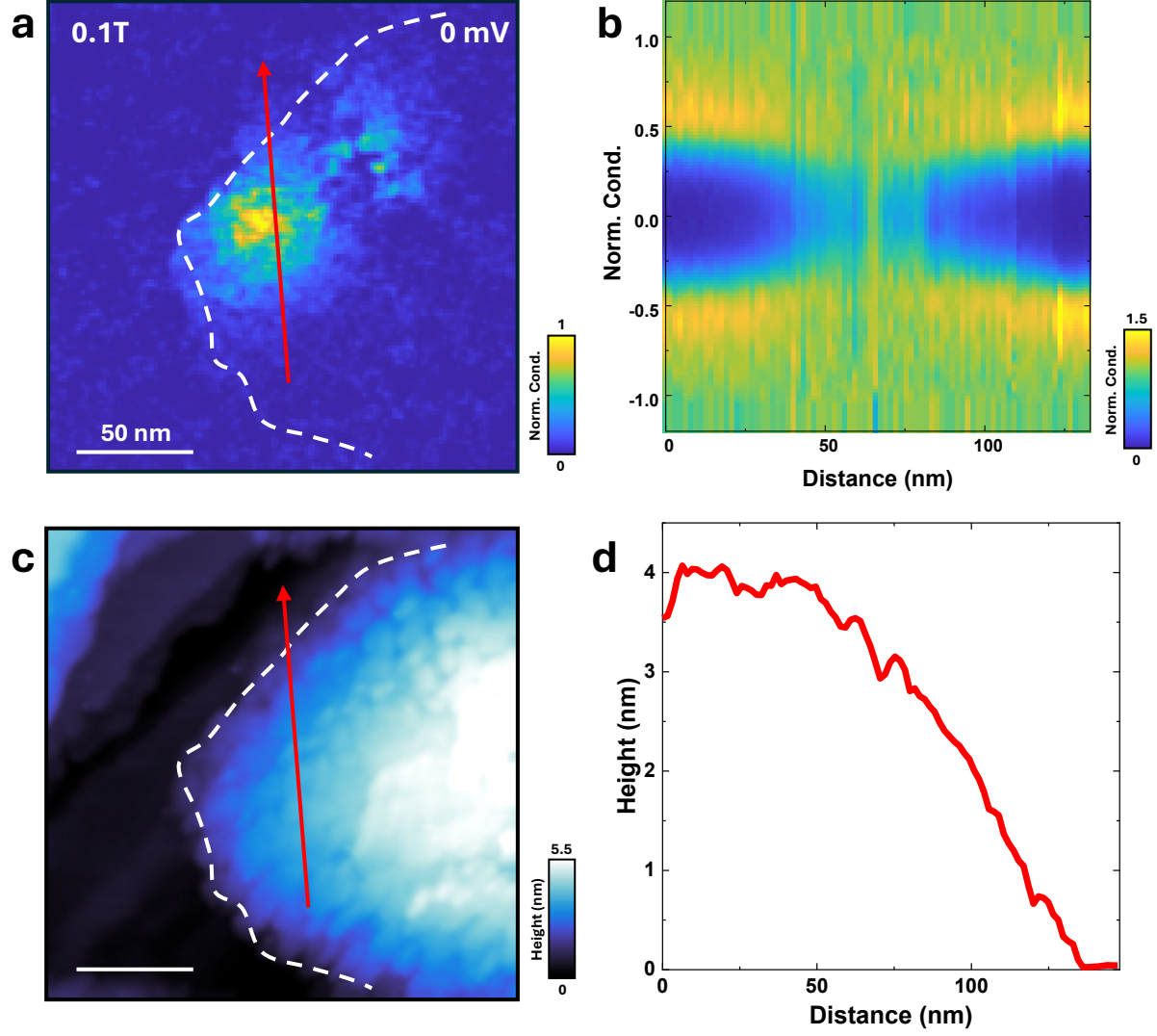


Figure 6. (a) Zero-bias conductance map obtained on a single vortex. Dashed line shows the contour separating a nanometer-sized flake (right side of the dashed line) from atomically flat terraces (left side of the dashed line). Color scale is shown on the bottom right. White scale bar is 50 nm long. (b) Tunneling conductance vs bias voltage along the red arrow in (a). (c) STM topography of the same field of view as in (a). Note the presence of atomic steps on the top left corner, having no significant influence on the zero bias tunneling conductance. (d) Height profile along the red arrow in (c). We set the height at zero on the atomically flat area.

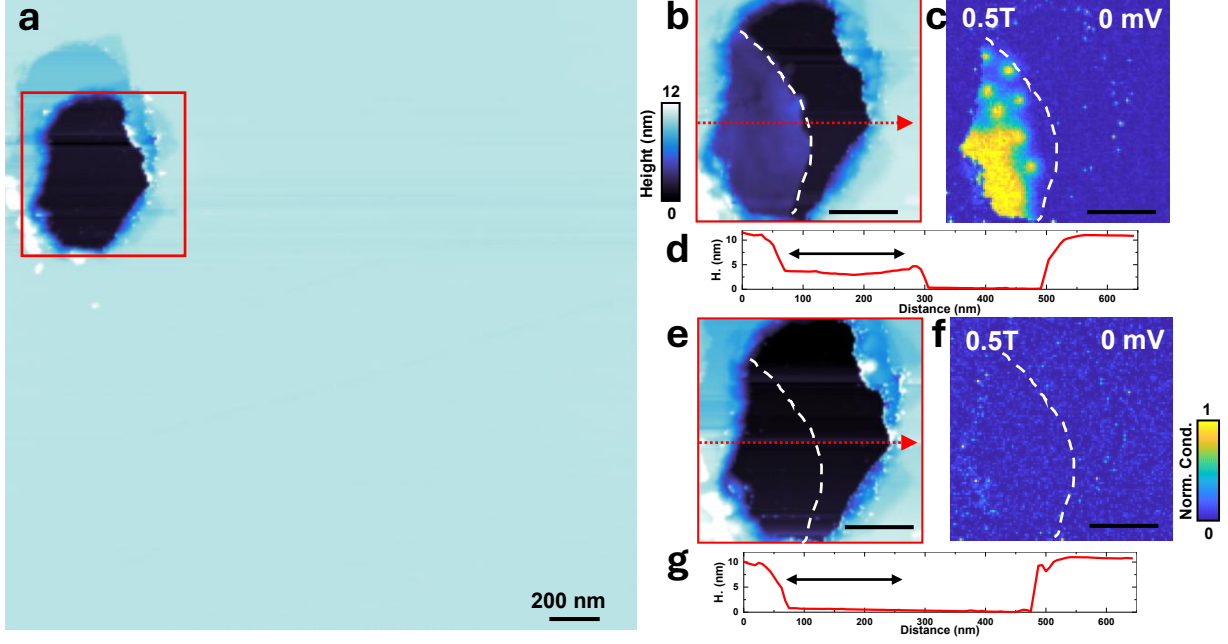


Figure 7. (a) Large scale STM topography of an atomically flat area ($2.5 \mu\text{m} \times 2.5 \mu\text{m}$). Notice the presence of a hole like structure on the top left part of this area. The hole is approximately 10 nm deep. (b) STM topography image of the top left area of (a). Within the hole, we find a nanometer-sized flake. The white dashed line shows the separation between flake (left side) and the atomically flat terrace (right side) within the hole. (c) Tunneling conductance map at zero bias in the same field of view as in (b). We observe a few vortices on the nanometer-sized flake. The intervortex distance is as expected for the applied magnetic field (0.5 T). (d) Height profile along the red dashed line in (b). (e) STM topography map of the same area as in (c), but after several scans. We see now that the surface within the hole is atomically flat. The interaction between tip and sample removed the rough area shown in (b). (f) Tunneling conductance map at zero bias on the same field of view as in (e). We can no longer identify vortices, showing that the vortex lattice in the whole field of view is now mobile. (g) Height profile along the red dashed line in (e).

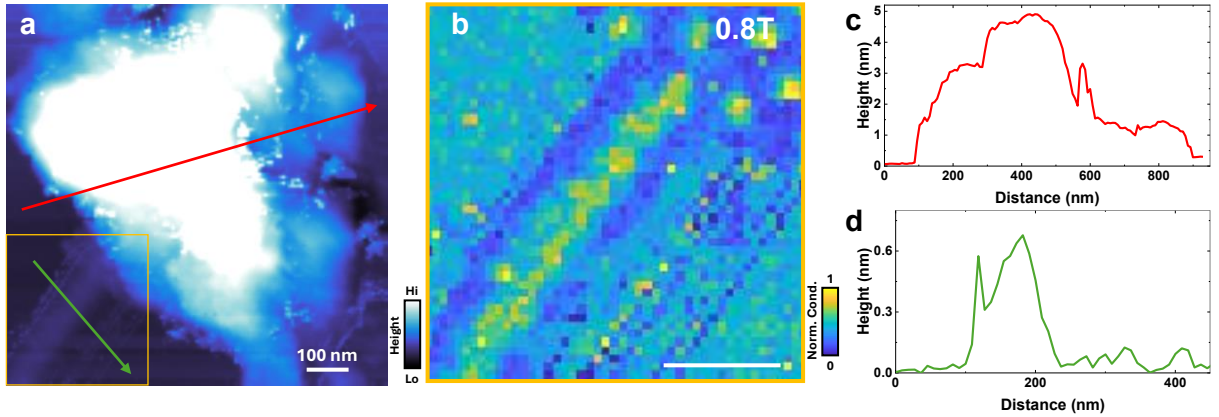


Figure 8. a) STM topography of the same field of view shown in Fig. 3 (e,f) of the main text. White line corresponds to 100 nm in size. (b) Zero-bias tunneling conductance map showing a zoom on the orange square in (a) at 0.8 T. This is the left bottom part of the figure shown in Fig. 3(e) of the main text. We see a row of a finite density of states, which we attribute to vortices moving along an elongated nanometer-sized flake. (c,d) Profiles of the topography corresponding along the red (c) and green (d) arrows shown in (a). We note that the height of the nanometer-sized flake along (d) is an order of magnitude smaller than the one shown in (c), enabling vortex mobility on the corresponding area.

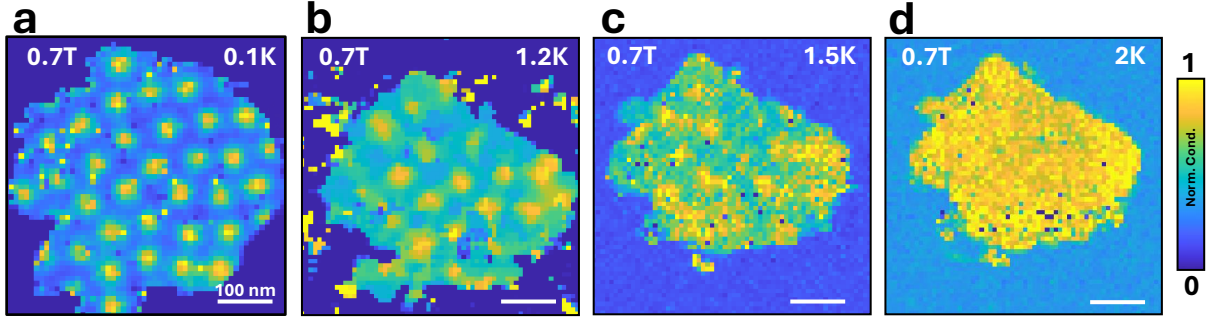


Figure 9. Zero-bias tunneling conductance map of the vortex lattice at 0.7 T in the same field of view as a function of temperature at 0.1 K (a), 1.2 K (b), 1.5 K (c), and 2 K (d). The area where we can observe the vortex lattice shows a strong roughness. Due to interaction with the tip, this area becomes slightly smaller with scanning. White scale bars are shown at the bottom and correspond to 100 nm in all images. The color scale is shown at the right and is the same for all images. We observe that the vortices increase considerably their mobility with increasing temperature.

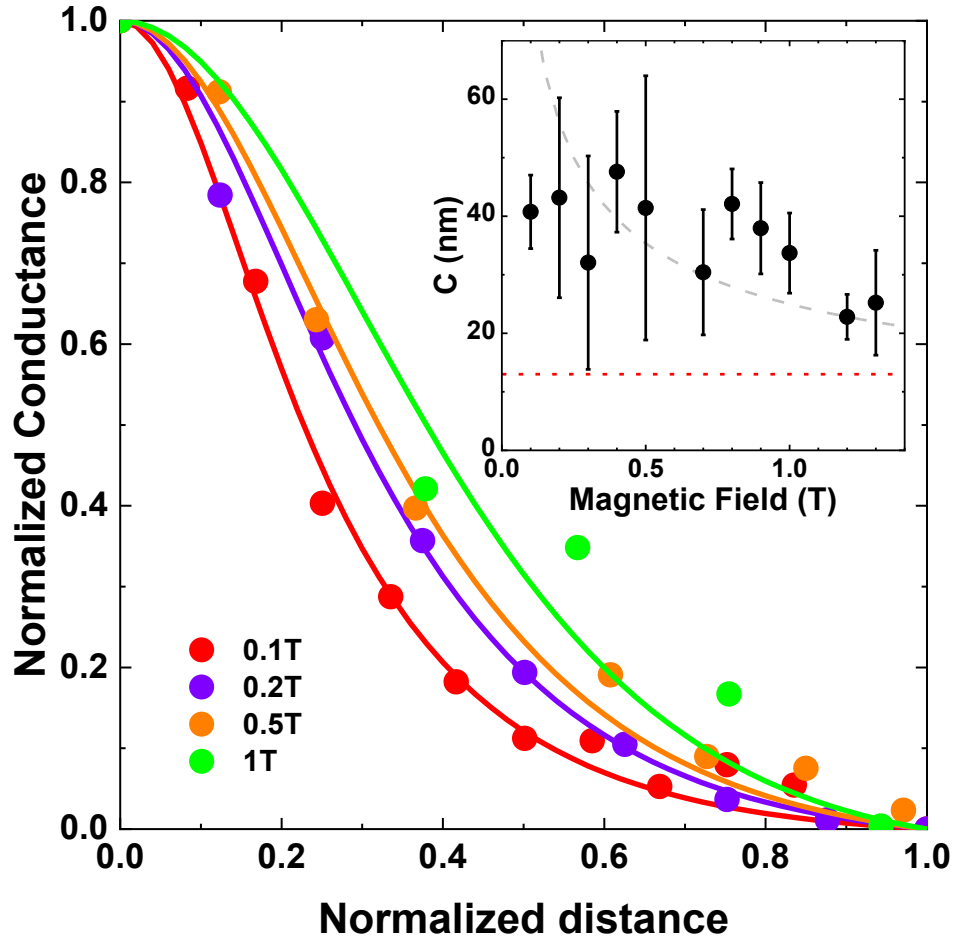


Figure 10. In the main panel we show by colored points the radially-averaged tunneling conductance normalized to its value in and outside vortex cores, following Ref. [82], for the values of the magnetic field shown in the legend. The colored lines are fits to the model of Ref. [82]. In the inset we show as dots the magnetic field dependence of the vortex core size C , defined as in Ref. [82]. The horizontal dotted line shows $\xi_{a,b} \sim 13$ nm. Dashed grey line indicates the expected vortex core size behaviour with field $\propto 1/\sqrt{H}$ for a superconductor in the clean limit [82].

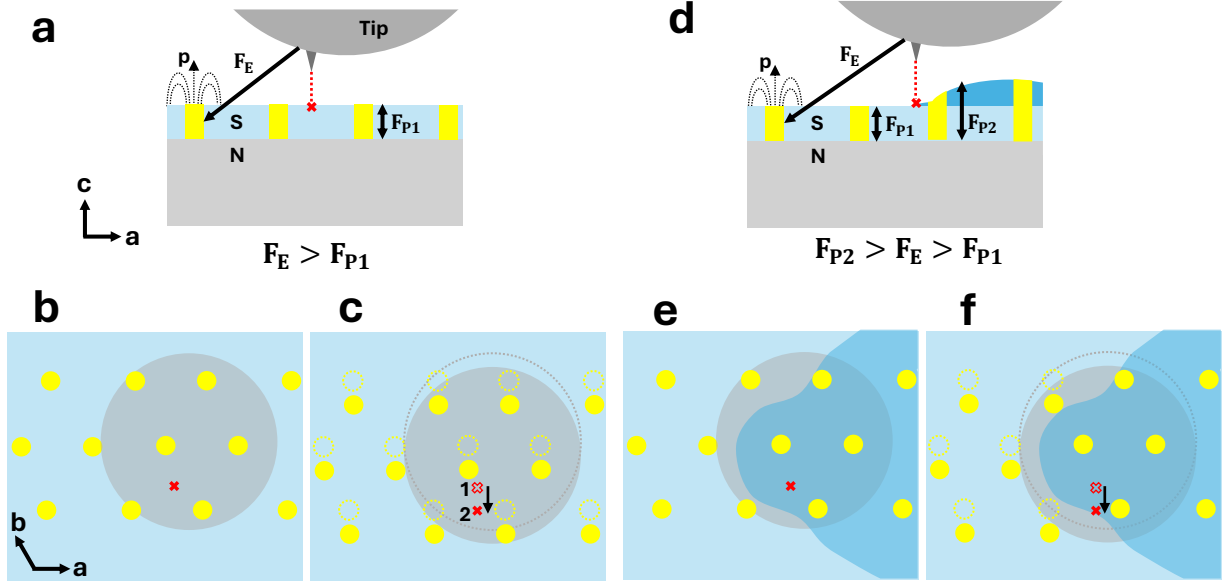


Figure 11. (a) Schematic lateral view of the STM measurement of the vortex lattice on a flat defect-free region. Superconducting topmost layer appears as light blue, the bulk normal metal as light grey and the tip as dark grey. Vortices appear as yellow. The red cross represents the position where the tunneling is measured. Black arrows represent schematically the electrostatic interaction between the tip and a vortex (F_E) and the pinning force (F_P). We schematically represent the electric dipole p appearing on vortices[39] as a dashed arrow. (b,c) Vortex lattice in two instances of the STM sweep on an atomically flat surface. The tip moves from top to the bottom following the black arrow in (c). Due to the interaction between the tip and the vortex lattice, the vortex lattice moves together with the tip. (d) Schematic view of the same arrangement as in (b,c), but now with an area on a nanometer-sized flake at the right. There are now two pinning forces, the one on the nanometer-sized flake (F_{P2}) being larger than the one on flat surfaces (F_{P1}). (e,f) Two instances of the tip's motion. Vortices on the nanometer-sized flake remain fixed and do not move with the tip, while those lying on atomically flat areas move.

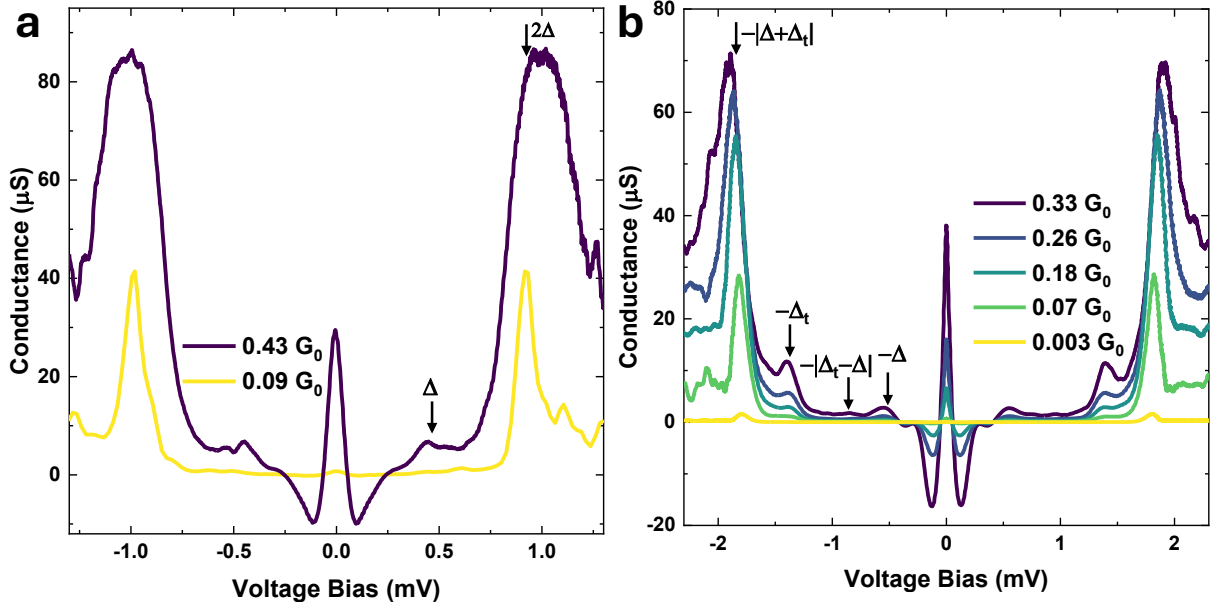


Figure 12. (a) Tunneling conductance obtained after picking a loose piece of γ -PtBi₂ with the tip. (b) Tunneling conductance obtained with a tip of Pb. The normal state tunneling conductance is provided in the legend in units of the quantum of conductance $G_0 = \frac{2e^2}{h} = 7.74810^{-5}$ S. Black arrows mark features related to the gap of the different electrodes and are discussed in the text.

-
- [1] B. Yan and C. Felser, Topological Materials: Weyl Semimetals, *Annual Review of Condensed Matter Physics* **8**, 337 (2017).
- [2] N. P. Armitage, E. J. Mele, and A. Vishwanath, Weyl and Dirac semimetals in three-dimensional solids, *Rev. Mod. Phys.* **90**, 015001 (2018).
- [3] G. E. Volovik, Fermion zero modes on vortices in chiral superconductors, *Journal of Experimental and Theoretical Physics Letters* **70**, 609 (1999).
- [4] L. Fu and C. L. Kane, Superconducting proximity effect and Majorana fermions at the surface of a topological insulator, *Phys. Rev. Lett.* **100**, 096407 (2008).
- [5] C. W. J. Beenakker, P. Baireuther, Y. Herasymenko, I. Adagideli, L. Wang, and A. R. Akhmerov, Deterministic creation and braiding of chiral edge vortices, *Phys. Rev. Lett.* **122**, 146803 (2019).
- [6] C. Beenakker, Search for Majorana fermions in superconductors, *Annual Review of Condensed Matter Physics* **4**, 113 (2013).
- [7] J. Alicea, New directions in the pursuit of Majorana fermions in solid state systems, *Reports on Progress in Physics* **75**, 076501 (2012).
- [8] H.-H. Sun and J.-F. Jia, Detection of Majorana zero mode in the vortex, *npj Quantum Materials* **2**, 34 (2017).
- [9] A. Nomani and P. Hosur, Intrinsic surface superconducting instability in type-I Weyl semimetals, *Phys. Rev. B* **108**, 165144 (2023).
- [10] X. Bai, W. LiMing, and T. Zhou, Superconductivity in Weyl semimetals with time reversal symmetry, *New Journal of Physics* **27**, 013003 (2025).
- [11] K. Mæland, M. Bahari, and B. Trauzettel, Phonon-mediated intrinsic topological superconductivity in Fermi arcs (2025), arXiv:2506.03250 [cond-mat.supr-con].
- [12] A. Kuibarov, O. Suvorov, R. Vocaturo, A. Fedorov, R. Lou, L. Merkwitz, V. Voroshnin, J. I. Facio, K. Koepernik, A. Yaresko, G. Shipunov, S. Aswartham, J. v. d. Brink, B. Büchner, and S. Borisenko, Evidence of superconducting Fermi arcs, *Nature* **626**, 294 (2024).
- [13] J. Zabala, V. F. Correa, F. J. Castro, and P. Pedrazzini, Enhanced weak superconductivity in trigonal γ -PtBi₂, *Journal of Physics: Condensed Matter* **36**, 285701 (2024).
- [14] D. L. Bashlakov, O. E. Kvitnitskaya, G. Shipunov, S. Aswartham, O. D. Feya, D. V. Efremov, B. Büchner, and Y. G. Naidyuk, Electron-phonon interaction and point contact enhanced superconductivity in trigonal PtBi₂, *Low Temperature Physics* **48**, 747 (2022).
- [15] S. Schimmel, Y. Fasano, S. Hoffmann, J. Besproswanny, L. T. Corredor Bohorquez, J. Puig, B.-C. Elshalem, B. Kalisky, G. Shipunov, D. Baumann, S. Aswartham, B. Büchner, and C. Hess, Surface superconductivity in the topological Weyl semimetal t-PtBi₂, *Nature Communications* **15**, 9895 (2024).
- [16] Y. Guo, J. Yan, W.-H. Dong, Y. Li, Y. Peng, X. Di, C. Li, Z. Wang, Y. Xu, P. Tang, Y. Yao, W. Duan, Q.-K. Xue, and W. Li, Topological surface states in γ -PtBi₂ evidenced by scanning tunneling microscopy (2025), arXiv:2505.10808 [cond-mat.supr-con].
- [17] S. Hoffmann, S. Schimmel, R. Vocaturo, J. Puig, G. Shipunov, O. Janson, S. Aswartham, D. Baumann, B. Büchner, J. v. d. Brink, Y. Fasano, J. I. Facio, and C. Hess, Fermi arcs dominating the electronic surface properties of trigonal PtBi₂, *Advanced Physics Research* **4**, 2400150 (2025).
- [18] G. Shipunov, I. Kovalchuk, B. R. Piening, V. Labracherie, A. Veyrat, D. Wolf, A. Lubk, S. Subakti, R. Giraud, J. Dufouleur, S. Shokri, F. Caglieris, C. Hess, D. V. Efremov, B. Büchner, and S. Aswartham, Polymorphic PtBi₂: Growth, structure, and superconducting properties, *Phys. Rev. Mater.* **4**, 124202 (2020).
- [19] W. Gao, X. Zhu, F. Zheng, M. Wu, J. Zhang, C. Xi, P. Zhang, Y. Zhang, N. Hao, W. Ning, and M. Tian, A possible candidate for triply degenerate point fermions in trigonal layered PtBi₂, *Nature Communications* **9**, 3249 (2018).
- [20] E. O'Leary, Z. Li, L.-L. Wang, B. Schruck, A. Eaton, P. C. Canfield, and A. Kaminski, Topography of Fermi arcs in t-PtBi₂ using high resolution angle-resolved photoemission spectroscopy (2025), arXiv:2503.08841 [cond-mat.mes-hall].
- [21] B. Wu, V. Barrena, H. Suderow, and I. Guillaón, Huge linear magnetoresistance due to open orbits in γ -PtBi₂, *Phys. Res.* **2**, 022042 (2020).
- [22] A. Veyrat, V. Labracherie, D. L. Bashlakov, F. Caglieris, J. I. Facio, G. Shipunov, T. Charvin, R. Acharya, Y. Naidyuk, R. Giraud, J. van den Brink, B. Büchner, C. Hess, S. Aswartham, and J. Dufouleur, Berezinskii-Kosterlitz-Thouless transition in the type-I Weyl semimetal PtBi₂, *Nano Letters* **23**, 1229 (2023).
- [23] J. Wang, X. Chen, Y. Zhou, C. An, Y. Zhou, C. Gu, M. Tian, and Z. Yang, Pressure-induced superconductivity in trigonal layered PtBi₂ with triply degenerate point fermions, *Phys. Rev. B* **103**, 014507 (2021).
- [24] J. Besproswanny, S. Schimmel, Y. Fasano, G. Shipunov, S. Aswartham, D. Baumann, B. Büchner, and C. Hess, Temperature dependence of surface superconductivity in t-PtBi₂ (2025), arXiv:2507.10187 [cond-mat.supr-con].
- [25] See supplemental material [url] for additional details and experiments, which includes references [60–94].
- [26] H. Suderow, I. Guillaón, and S. Vieira, Compact very low temperature scanning tunneling microscope with mechanically driven horizontal linear positioning stage, *Review of Scientific Instruments* **82**, 033711 (2011).
- [27] M. Fernández-Lomana, B. Wu, F. Martín-Vega, R. Sánchez-Barquilla, R. Álvarez Montoya, J. M. Castilla, J. Navarrete, J. R. Marijuan, E. Herrera, H. Suderow, and I. Guillaón, Millikelvin scanning tunneling microscope at 20/22 T with a graphite enabled stick-slip approach and an energy resolution below 8 μ eV: Application to conductance quantization at 20 T in single atom point contacts of Al and Au and to the charge density wave of 2H-NbSe₂, *Review of Scientific Instruments* **92**, 093701 (2021).
- [28] F. Martín-Vega, V. Barrena, R. Sánchez-Barquilla, M. Fernández-Lomana, J. Benito Llorens, B. Wu, A. Fente, D. Perconte Duplain, I. Horcas, R. López, J. Blanco, J. A. Higuera, S. Mañas-Valero, N. H. Jo, J. Schmidt, P. C. Canfield, G. Rubio-Bollinger, J. G. Rodrigo, E. Herrera, I. Guillaón, and H. Suderow, Simplified feedback control system for scanning tunneling microscopy, *Review of Scientific Instruments* **92**, 103705 (2021).
- [29] I. Horcas, R. Fernandez, J. M. Gomez-Rodriguez, J. Colchero, J. Gomez-Herrero, and A. M. Baro, WSXM:

- A software for scanning probe microscopy and a tool for nanotechnology, *Rev. Sci. Instrum.* **78**, 013705 (2007).
- [30] LowTemperaturesUAM, GitHub, <https://github.com/LowTemperaturesUAM>.
- [31] E. Herrera, I. Guillamón, J. A. Galvis, A. Correa, A. Fente, R. F. Luccas, F. J. Mompeán, M. García-Hernández, S. Vieira, J. P. Brison, and H. Suderow, Magnetic field dependence of the density of states in the multiband superconductor β -Bi₂Pd, *Phys. Rev. B* **92**, 054507 (2015).
- [32] E. Herrera, B. Wu, E. O’Leary, A. M. Ruiz, M. Águeda, P. G. Talavera, V. Barrena, J. Azpeitia, C. Munuera, M. García-Hernández, L.-L. Wang, A. Kaminski, P. C. Canfield, J. J. Baldoví, I. Guillamón, and H. Suderow, Band structure, superconductivity, and polytypism in AuSn₄, *Phys. Rev. Mater.* **7**, 024804 (2023).
- [33] F. Martín-Vega, E. Herrera, B. Wu, V. Barrena, F. Mompeán, M. García-Hernández, P. C. Canfield, A. M. Black-Schaffer, J. J. Baldoví, I. Guillamón, and H. Suderow, Superconducting density of states and band structure at the surface of the candidate topological superconductor Au₂Pb, *Phys. Rev. Res.* **4**, 023241 (2022).
- [34] I. Guillamón, H. Suderow, S. Vieira, L. Cario, P. Diener, and P. Rodière, Superconducting density of states and vortex cores of 2H-NbS₂, *Phys. Rev. Lett.* **101**, 166407 (2008).
- [35] A. Fente, W. R. Meier, T. Kong, V. G. Kogan, S. L. Bud’ko, P. C. Canfield, I. Guillamón, and H. Suderow, Influence of multiband sign-changing superconductivity on vortex cores and vortex pinning in stoichiometric high- T_c CaKFe₄As₄, *Phys. Rev. B* **97**, 134501 (2018).
- [36] P. García Talavera, J. A. Moreno, E. Herrera, A. I. Buzdin, S. L. Bud’ko, P. C. Canfield, I. Guillamón, and H. Suderow, Superconducting density of states of PtPb₄, *Journal of Superconductivity and Novel Magnetism* **38**, 158 (2025).
- [37] G. Blatter, M. V. Feigel’man, V. B. Geshkenbein, A. I. Larkin, and V. M. Vinokur, Vortices in high-temperature superconductors, *Rev. Mod. Phys.* **66**, 1125 (1994).
- [38] E. H. Brandt, The flux-line lattice in superconductors, *Reports on Progress in Physics* **58**, 1465 (1995).
- [39] G. Blatter, M. Feigel’man, V. Geshkenbein, A. Larkin, and A. van Otterlo, Electrostatics of vortices in Type-II superconductors, *Phys. Rev. Lett.* **77**, 566 (1996).
- [40] D. I. Khomskii and A. Freimuth, Charged vortices in high temperature superconductors, *Phys. Rev. Lett.* **75**, 1384 (1995).
- [41] S. K. Sahu, S. Mandal, S. Ghosh, M. M. Deshmukh, and V. Singh, Superconducting vortex-charge measurement using cavity electromechanics, *Nano Letters* **22**, 1665 (2022), pMID: 35147441.
- [42] M. Machida and T. Koyama, Vortex charge in the superconducting state, *Physica C: Superconductivity* **378-381**, 443 (2002).
- [43] M. Fauré, B. Lounis, and A. I. Buzdin, Single-molecule spectroscopy as a possible tool to study the electric field in superconductors, *Europhysics Letters* **77**, 17005 (2007).
- [44] M. Ohuchi, H. Ueki, and T. Kita, Charging in the vortex lattice of type-II superconductors, *Phys. Rev. B* **105**, 064514 (2022).
- [45] O. B. Hyun, D. K. Finnemore, L. Schwartzkopf, and J. R. Clem, Elementary pinning force for a superconducting vortex, *Phys. Rev. Lett.* **58**, 599 (1987).
- [46] J. T. Zhang, J. Kim, M. Huefner, C. Ye, S. Kim, P. C. Canfield, R. Prozorov, O. M. Auslaender, and J. E. Hoffman, Single-vortex pinning and penetration depth in superconducting NdFeAsO_{1-x}F_x, *Phys. Rev. B* **92**, 134509 (2015).
- [47] I. Guillamón, H. Suderow, A. Fernández-Pacheco, J. Sesé, R. Córdoba, J. M. De Teresa, M. R. Ibarra, and S. Vieira, Direct observation of melting in a two-dimensional superconducting vortex lattice, *Nature Physics* **5**, 651 (2009).
- [48] R. Duhan, S. Sengupta, R. Tomar, S. Basistha, V. Bagwe, C. Dasgupta, and P. Raychaudhuri, Structure and dynamics of a pinned vortex liquid in a superconducting Re₆Zr thin film, *Phys. Rev. B* **108**, L180503 (2023).
- [49] R. Duhan, S. Sengupta, J. Jesudasan, S. Basistha, and P. Raychaudhuri, Inverse melting and re-entrant transformations of the vortex lattice in amorphous Re₆Zr thin film, *Nature Communications* **16**, 2100 (2025).
- [50] H. Suderow, I. Guillamón, J. G. Rodrigo, and S. Vieira, Imaging superconducting vortex cores and lattices with a scanning tunneling microscope, *Superconductor Science and Technology* **27**, 063001 (2014).
- [51] J.-Y. Ge, V. N. Gladilin, J. Tempere, C. Xue, J. T. Devreese, J. Van de Vondel, Y. Zhou, and V. V. Moshchalkov, Nanoscale assembly of superconducting vortices with scanning tunnelling microscope tip, *Nature Communications* **7**, 13880 (2016).
- [52] L. Yang, L. Li, Z.-M. Yu, M. Wu, and Y. Yao, Two-dimensional topological ferroelectric metal with giant shift current, *Phys. Rev. Lett.* **133**, 186801 (2024).
- [53] C. Caroli, P. De Gennes, and J. Matricon, Bound fermion states on a vortex line in a type II superconductor, *Physics Letters* **9**, 307 (1964).
- [54] H. F. Hess, R. B. Robinson, and J. V. Waszczak, Vortex-core structure observed with a scanning tunneling microscope, *Phys. Rev. Lett.* **64**, 2711 (1990).
- [55] S. Park, V. Barrena, S. Mañas-Valero, J. J. Baldoví, A. Fente, E. Herrera, F. Mompeán, M. García-Hernández, Á. Rubio, E. Coronado, I. Guillamón, A. L. Yeyati, and H. Suderow, Coherent coupling between vortex bound states and magnetic impurities in 2d layered superconductors, *Nature Communications* **12**, 4668 (2021).
- [56] N. Hayashi, T. Isoshima, M. Ichioka, and K. Machida, Low-lying quasiparticle excitations around a vortex core in quantum limit, *Phys. Rev. Lett.* **80**, 2921 (1998).
- [57] C. Renner, A. D. Kent, P. Niedermann, O. Fischer, and F. Lévy, Scanning tunneling spectroscopy of a vortex core from the clean to the dirty limit, *Phys. Rev. Lett.* **67**, 1650 (1991).
- [58] Y. Masaki and Y. Kato, Charged and uncharged vortices in quasiclassical theory, *Journal of Physics: Conference Series* **969**, 012054 (2018).
- [59] Y. Masaki, Vortex charges and impurity effects based on quasiclassical theory in an *s*-wave and a chiral *p*-wave superconductor, *Phys. Rev. B* **99**, 054512 (2019).
- [60] P. C. Canfield, T. Kong, U. S. Kaluarachchi, and N. H. Jo, Use of frit-disc crucibles for routine and exploratory solution growth of single crystalline samples, *Philosophical Magazine* **96**, 84 (2016).
- [61] P. C. Canfield, Canfield crucible set (2015).
- [62] P. C. Canfield, New materials physics, *Reports on Progress in Physics* **83**, 016501 (2019).
- [63] H. Okamoto, The Bi-Pt (Bismuth-Platinum) system, *Journal of Phase Equilibria* **12**, 207 (1991).

- [64] J. G. Rodrigo, H. Suderow, and S. Vieira, On the use of STM superconducting tips at very low temperatures, *The European Physical Journal B - Condensed Matter and Complex Systems* **40**, 483 (2004).
- [65] J. G. Rodrigo, H. Suderow, S. Vieira, E. Bascones, and F. Guinea, Superconducting nanostructures fabricated with the scanning tunnelling microscope, *Journal of Physics: Condensed Matter* **16**, R1151 (2004).
- [66] P. Hohenberg and W. Kohn, Inhomogeneous electron gas, *Phys. Rev.* **136**, B864 (1964).
- [67] W. Kohn and L. J. Sham, Self-consistent equations including exchange and correlation effects, *Phys. Rev.* **140**, A1133 (1965).
- [68] J. P. Perdew, K. Burke, and M. Ernzerhof, Generalized gradient approximation made simple, *Phys. Rev. Lett.* **78**, 1396 (1997).
- [69] P. E. Blöchl, Projector augmented-wave method, *Phys. Rev. B* **50**, 17953 (1994).
- [70] G. Kresse and J. Furthmüller, Efficient iterative schemes for ab initio total-energy calculations using a plane-wave basis set, *Phys. Rev. B* **54**, 11169 (1996).
- [71] G. Kresse and J. Furthmüller, Efficiency of ab-initio total energy calculations for metals and semiconductors using a plane-wave basis set, *Computational Materials Science* **6**, 15 (1996).
- [72] H. J. Monkhorst and J. D. Pack, Special points for Brillouin-zone integrations, *Phys. Rev. B* **13**, 5188 (1976).
- [73] N. Marzari and D. Vanderbilt, Maximally localized generalized Wannier functions for composite energy bands, *Phys. Rev. B* **56**, 12847 (1997).
- [74] I. Souza, N. Marzari, and D. Vanderbilt, Maximally localized wannier functions for entangled energy bands, *Phys. Rev. B* **65**, 035109 (2001).
- [75] N. Marzari, A. A. Mostofi, J. R. Yates, I. Souza, and D. Vanderbilt, Maximally localized wannier functions: Theory and applications, *Rev. Mod. Phys.* **84**, 1419 (2012).
- [76] H. Inoue, A. Gyenis, Z. Wang, J. Li, S. W. Oh, S. Jiang, N. Ni, B. A. Bernevig, and A. Yazdani, Quasiparticle interference of the Fermi arcs and surface-bulk connectivity of a Weyl semimetal, *Science* **351**, 1184 (2016).
- [77] M. P. L. Sancho, J. M. L. Sancho, and J. Rubio, Quick iterative scheme for the calculation of transfer matrices: application to Mo (100), *Journal of Physics F: Metal Physics* **14**, 1205 (1984).
- [78] M. P. L. Sancho, J. M. L. Sancho, J. M. L. Sancho, and J. Rubio, Highly convergent schemes for the calculation of bulk and surface Green functions, *Journal of Physics F: Metal Physics* **15**, 851 (1985).
- [79] Q. Wu, S. Zhang, H.-F. Song, M. Troyer, and A. A. Soluyanov, Wanniertools: An open-source software package for novel topological materials, *Computer Physics Communications* **224**, 405 (2018).
- [80] S. D. Edkins, A. Kostin, K. Fujita, A. P. Mackenzie, H. Eisaki, S. Uchida, S. Sachdev, M. J. Lawler, E.-A. Kim, J. C. S. Davis, and M. H. Hamidian, Magnetic field-induced pair density wave state in the cuprate vortex halo, *Science* **364**, 976 (2019).
- [81] K. Matsuba, H. Sakata, N. Kosugi, H. Nishimori, and N. Nishida, Ordered vortex lattice and intrinsic vortex core states in $\text{Bi}_2\text{Sr}_2\text{CaCu}_2\text{O}_x$ Studied by Scanning Tunneling Microscopy and Spectroscopy, *Journal of the Physical Society of Japan* **72**, 2153 (2003).
- [82] A. Fente, E. Herrera, I. Guillaumon, H. Suderow, S. Mañas Valero, M. Galbiati, E. Coronado, and V. G. Kogan, Field dependence of the vortex core size probed by scanning tunneling microscopy, *Phys. Rev. B* **94**, 014517 (2016).
- [83] P. G. de Gennes, Behavior of dirty superconductors in high magnetic fields, *Physik der kondensierten Materie* **3**, 79 (1964).
- [84] J. Tersoff and D. R. Hamann, Theory of the scanning tunneling microscope, *Phys. Rev. B* **31**, 805 (1985).
- [85] J. Y. Park, G. M. Sacha, M. Enachescu, D. F. Ogletree, R. A. Ribeiro, P. C. Canfield, C. J. Jenks, P. A. Thiel, J. J. Sáenz, and M. Salmeron, Sensing dipole fields at atomic steps with combined scanning tunneling and force microscopy, *Phys. Rev. Lett.* **95**, 136802 (2005).
- [86] I. Guillaumon, Models and mountains, *Nature Physics* **17**, 1077 (2021).
- [87] Y. L. Wang, H.-J. Gao, H. M. Guo, H. W. Liu, I. G. Batyrev, W. E. McMahon, and S. B. Zhang, Tip size effect on the appearance of a STM image for complex surfaces: Theory versus experiment for $\text{Si}(111)-(7 \times 7)$, *Phys. Rev. B* **70**, 073312 (2004).
- [88] C. R. Ast, B. Jäck, J. Senkpiel, M. Eltschka, M. Etzkorn, J. Ankerhold, and K. Kern, Sensing the quantum limit in scanning tunnelling spectroscopy, *Nature Communications* **7**, 13009 (2016).
- [89] A. Sadeghi, A. Baratoff, and S. Goedecker, Electrostatic interactions with dielectric samples in scanning probe microscopies, *Phys. Rev. B* **88**, 035436 (2013).
- [90] M. McEllistrem, G. Haase, D. Chen, and R. J. Hamers, Electrostatic sample-tip interactions in the scanning tunneling microscope, *Phys. Rev. Lett.* **70**, 2471 (1993).
- [91] Y. Noat, V. Cherkez, C. Brun, T. Cren, C. Carillet, F. Debontridder, K. Ilin, M. Siegel, A. Semenov, H.-W. Hübers, and D. Roditchev, Unconventional superconductivity in ultrathin superconducting NbN films studied by scanning tunneling spectroscopy, *Phys. Rev. B* **88**, 014503 (2013).
- [92] S. V. Postolova, A. Y. Mironov, V. Barrena, J. Benito-Llorens, J. G. Rodrigo, H. Suderow, M. R. Baklanov, T. I. Baturina, and V. M. Vinokur, Superconductivity in a disordered metal with Coulomb interactions, *Phys. Rev. Res.* **2**, 033307 (2020).
- [93] S. Dutta, J. Jesudasan, and P. Raychaudhuri, Magnetic field induced transition from a vortex liquid to Bose metal in ultrathin a -MoGe thin film, *Phys. Rev. B* **105**, L140503 (2022).
- [94] M. Ternes, W.-D. Schneider, J.-C. Cuevas, C. P. Lutz, C. F. Hirjibehedin, and A. J. Heinrich, Subgap structure in asymmetric superconducting tunnel junctions, *Phys. Rev. B* **74**, 132501 (2006).